Research on Delamination Damage Localization of CFRP Bending Plate Using Lamb Wave

Quanpeng Yu , Shiyuan Zhou * , Yuhan Cheng , Yao Deng

Posted Date: 22 April 2024

doi: 10.20944/preprints202404.1308.v1

Keywords: Lamb wave; CFRP bending plate; delamination damage localization; IRAPID algorithm

 doi:10.20944/preprints202404.1308.v1

Article

Research on Delamination Damage Localization of CFRP Bending Plate Using Lamb Wave

Quanpeng Yu, Shiyuan Zhou *, Yuhan Cheng and Yao Deng

School of Mechanical Engineering, Beijing Institute of Technology, No. 5, Zhongguancun South Street, Haidian District, Beijing 100081, China; yuubit@163.com (Q.Y.); aslslcyh@163.com (Y.C.); 18701200802@163.com (Y.D.)

* Correspondence: zhoushy@bit.edu.cn; Tel.: +86-010-68912715

Abstract: Carbon fiber reinforced polymers (CFRP) are extensively employed in the aerospace industry due to their excellent properties. Delamination damage occurring at critical locations in CFRP can seriously reduce the safety of in-service components. The detection and localization of delamination damage using Lamb waves hold significant potential for widespread application in non-destructive testing. However, the choice of damage localization algorithm may produce different delamination damage localization results. This research presented an IRAPID (improved reconstruction algorithm for probabilistic inspection of defects) method derived from the ORAPID (original reconstruction algorithm for probabilistic inspection of defects) method, aiming to improve the accuracy and reliability of delamination damage localization. Three CFRP bending plates, including a healthy bending plate and two bending plates with delamination damage sizes of Φ20 mm and Φ40 mm, were prepared in the experiment, respectively. The detection experiment of the CFRP bending plate using lead zirconate titanate (PZT) as a transducer to excite and receive Lamb waves was conducted, and the influence of excitation signal frequency on the performance of the proposed method was discussed. Under the condition of excitation signal frequency of 220 ~ 320 kHz and step size of 10 kHz, the accuracy of the delamination damage localization method proposed in this paper was compared with that of the existing methods. The experimental results indicate that the IRAPID algorithm exhibits good stability in the localization of delamination damage across the frequency variations range considered. The localization error of the IRAPID algorithm for delamination damage is significantly lower than that of the DaS (delay-and-sum) algorithm and the ORAPID algorithm. As the size of the delamination damage increases, so does the localization error. The accuracy of delamination damage localization is lower in the X-axis direction than in the Y-axis direction. By averaging the localization results across various frequencies, we can mitigate the potential localization errors associated with single-frequency detection to a certain extent. For the localization of delamination damage, Lamb waves at multiple frequencies can be employed for detection, and the detection results at each frequency are averaged to enhance the reliability of localization.

Keywords: Lamb wave; CFRP bending plate; delamination damage localization; IRAPID algorithm

1. Introduction

CFRP exhibits a range of significant advantages, such as high specific strength, high specific stiffness, excellent design flexibility, outstanding damping performance, and prolonged fatigue life [1,2]. As a result, they are extensively employed in sectors like aerospace, military equipment, marine, and automotive industries [3–6]. In the manufacturing process of aerospace equipment, more than 50% of the components are made of CFRP. For instance, in the overall structure of the Boeing 787 Dreamliner, the proportion of CFRP used is as high as 57%, thereby achieving a fuel savings of 15-20% [7]. 53 % of the total volume of Airbus 350 WXB aircraft is made of CFRP, which reduces the aircraft's weight, thereby fuel consumption has been cut by nearly 25% [8]. In the field of aero-engines, the fan box and blades of the compressor cooler system of GE Aviation's GEnx series engines are made of CFRP, which not only reduces the weight of the fuselage by 180 kg but also reduces emissions by 15% and operating costs by 20% [9]. At the same time, CFRP also plays a vital role in

 doi:10.20944/preprints202404.1308.v1

component manufacturing for military equipment such as helmets, body armor, combat shields, and armored vehicles [10,11].

CFRP exhibits orthotropic properties, which make its failure modes potentially more complex and hidden than those of isotropic materials [12–15], such as matrix cracking, fiber breakage, and delamination [16], during production and service. Delamination is the most common and harmful failure mode [17,18]. The internal cause of delamination is the low transverse tensile strength and interlaminar shear strength of CFRP laminates [19], while the external cause is damage such as drilling [20–22] and impact [23]. In addition, fatigue further causes delamination expansion [24,25]. The occurrence and expansion of delamination significantly reduce the structure's stiffness, strength, and load-carrying capacity, resulting in a substantial reduction in the buckling load and compressive strength of CFRP laminates, which may ultimately cause catastrophic failure of CFRP structures [26]. However, delamination usually occurs inside CFRP structures and is hidden, which makes it challenging to detect delamination damage. Developing effective delamination detection techniques for CFRP structures is crucial for ensuring the safe and reliable realization of CFRP in various practical applications. Furthermore, CFRP is fabricated into various structural types to meet diverse engineering application needs, such as tubes [27], rods [28], beams [29], winglets [30], and bending structures [31]. As a relatively simple CFRP structure, bending components are widely used in aircraft, spacecraft, and ships [32,33]. Due to the characteristics of the CFRP bending structure, stress concentration is easy to occur at the bending areas, resulting in the emergence of delamination damage, which seriously affects the structure's safety.

As an active method for structural damage detection and health monitoring, Lamb waves possess advantages such as long propagation distance, low cost, and high sensitivity to delamination damage. It has emerged as one of the primary methods in the engineering detection field [34] and is extensively applied in CFRP material structural damage detection [35]. Scattering and reflection phenomena will occur when Lamb waves encounter delamination damage in CFRP [36,37]. Simultaneously, Lamb waves will be divided into two parts, which will propagate independently in the upper and lower sub-layers of the delamination area, and undergo modal transformation at the edge of the delamination [38,39]. Based on this property of the Lamb waves, delamination damage detection can be achieved. However, due to the dispersion characteristics of Lamb waves, their propagation process in CFRP becomes extremely complex. Each mode of Lamb waves propagates at varying velocities across different frequencies, which leads to deformation and amplitude reduction during the propagation of Lamb waves in CFRP, bringing potential challenges to the application of Lamb waves in engineering detection. Therefore, it is necessary to conduct research on the damage detection of CFRP structures based on Lamb waves.

Some scholars have utilized experimental methods, employing PZT as a transducer, to investigate the capability of Lamb waves in detecting delamination damage in CFRP laminated plates, and have accomplished the detection and localization of delamination damage [40,41]. Xiang Zhao et al. [42] compared and analyzed the effects of several tomography techniques, including filtered back-projection algorithm, algebraic reconstruction algorithm, and reconstruction algorithm for probabilistic inspection of damage, on composite material damage Lamb wave imaging. Liping Huang et al. [43] utilized the time reversibility of Lamb waves to propose an improved time reversal method for accurately locating impact damage in composite plates. Songlai Wang compared the influence of different patterns of PZT sensors, such as circular, square, and parallel arrays, on reconstruction image qualities of damage localization [44]. Jiahui Guo et al. [45] integrated probabilistic imaging algorithms and statistical methods to reduce the impact of composite anisotropy on the accuracy of damage detection. The matching pursuit decomposition algorithm was used to extract the accurate Lamb wave time of flight (ToF) for damage detection. The proposed algorithm can locate and quantify the damage of composite plates. The proposed algorithm can locate and quantify composite plate damage. Haode Huo [46] integrated the elliptical trajectory method and reconstruction algorithm for probabilistic inspection of defects in the Bayesian framework. This method combines multiple damage-sensitive features, and numerical and experimental studies have

 doi:10.20944/preprints202404.1308.v1

been conducted to verify the effectiveness of the proposed method for locating composite plate damage using Lamb waves. The proposed method produces more accurate and reliable results.

Based on the ORAPID algorithm, this study proposes an IRAPID algorithm. The Lamb wave detection experiment was carried out on CFRP bending plates with Φ20 mm and Φ40 mm delamination damage using PZT as the transducer. The influence of the excitation signal frequency on the proposed method's performance was discussed. Under the condition of excitation signal frequency of 220 ~ 320 kHz and step size of 10 kHz, the accuracy of the delamination damage localization method proposed in this paper was compared with that of existing DaS and ORAPID methods. The research results indicate that the method for delamination damage localization proposed in this paper exhibits good stability and accuracy.

2. Lamb Wave Localization Imaging Algorithm

The Lamb wave localization imaging algorithm is based on the principle that when the Lamb wave propagates in the waveguide structure and encounters damage, the damage can be regarded as a secondary wave source. The scattering of the Lamb wave occurs at the secondary wave source, and the scatter Lamb wave will continue to propagate in the waveguide structure, thus being caught by the receiving sensor. Lamb wave localization imaging can be performed based on the difference between the non-damage baseline signal and the signal with damage information.

2.1. DaS Algorithm

In the DaS algorithm, the detection area is discretized into regular grid nodes, and the grid nodes are assumed to be potential damage location points. The scattered wave's ToF of the actuator-damage-sensor propagation path is calculated, and the values of all scattered wave signals on the corresponding ToF are fused to obtain the damage probability value of the grid nodes in the detection area. Through a priori information such as wave velocity and position of the transducer, the calculation of the ToF of scattered wave signals at each grid node under a certain path is expressed as

$$t_{ij}^{R}(x,y)=\frac{\sqrt{\left(x-x_i\right)^2+\left(y-y_i\right)^2}}{V}+\frac{\sqrt{\left(x-x_j\right)^2+\left(y-y_j\right)^2}}{V}, \tag{1}$$

where (x, y) are the position coordinates of the grid nodes in the detection area. The variable $t_{ij}^{R}(x,y)$ is the ToF of the scattered wave signal with the grid node coordinates (x, y) on the path from the i th actuator to the j th sensor. V is the group velocity of the Lamb wave. As shown in Figure 1, $A(x_i,y_i)$ is the fixed position coordinate of the i th actuator, and $S(x_j,y_j)$ is the fixed position coordinate of the j th sensor. When $t_{ij}^{R}(x,y)$ is a constant value, the trajectory formed by the coordinates (x, y) satisfying Equation (1) is an ellipse, and the position coordinates of the actuator and the sensor are the two focuses of the ellipse. The coordinates (x, y) traverse the entire detection area with a certain step size, and the $t_{ij}^{R}(x,y)$ of each grid node under a certain path can be obtained.

The Lamb wave detection experiments were carried out on both non-damaged and damaged samples, and the resulting non-damaged and damaged signals are shown in Figure 2a,b, respectively. The scattered wave signal $S_S(t)$ obtained by subtracting the baseline signal $S_B(t)$ from the damage signal $S_D(t)$ is expressed as

$$S_S(t)=S_B(t)-S_D(t), \tag{2}$$

Preprints.org (www.preprints.org) | NOT PEER-REVIEWED | Posted: 22 April 2024 doi:10.20944/preprints202404.1308.v1

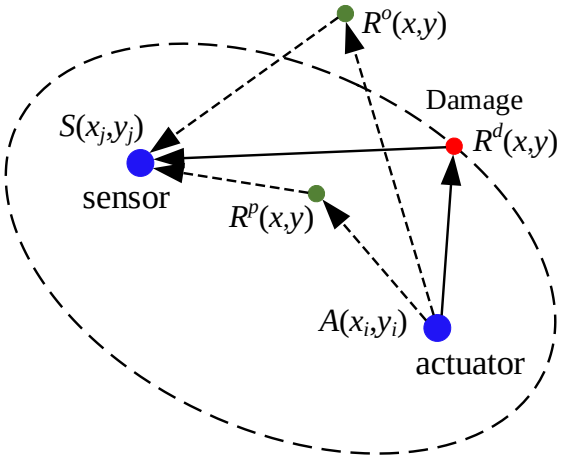

Figure 1. Imaging trajectory.

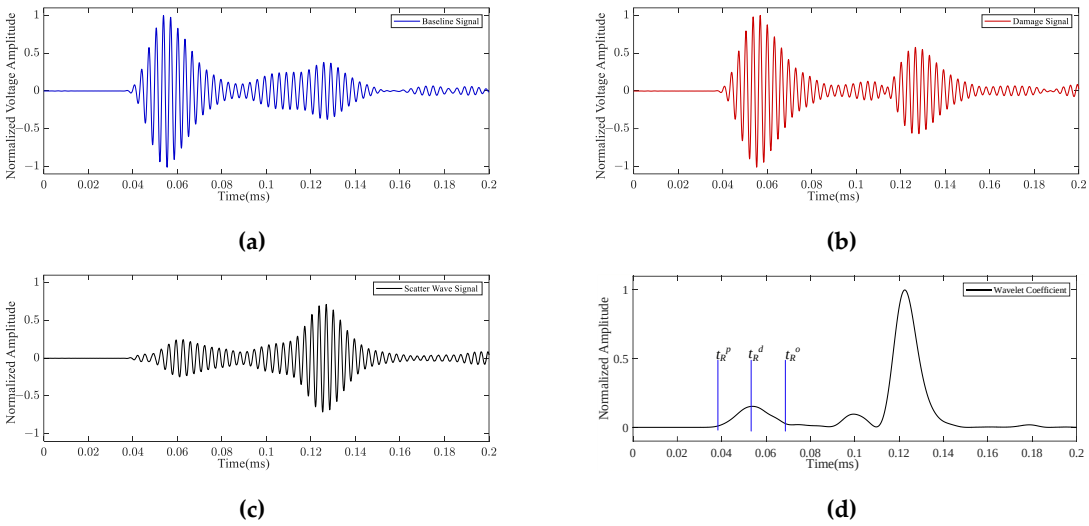

Figure 2. Lamb wave signal: (**a**) baseline signal; (**b**) damage signal; (**c**) scattered wave signal; (**d**) *CWTC*.

The scattered wave signal is shown in Figure 2c. The scattered wave signal was processed using continuous wavelet transform (*CWT*), and the resulting *CWT* coefficient (*CWTC*) is shown in Figure 2d. The *CWTC* value $CWTC(t_{ij}^R(x,y))$ of the scattered wave signal at the time $t_{ij}^R(x,y)$ was assigned to the corresponding grid node with coordinates (x, y). As shown in Figures 1 and 2d, when the selected detection area grid node $R^d(x,y)$ is located on the damage path, the calculated ToF is t_R^d, and the $CWTC(t_{ij}^R(x,y))$ reaches its maximum value at the moment t_R^d. However, when the selected detection area grid nodes $R^p(x,y)$ and $R^o(x,y)$ are not located on the damage path, the calculated ToF is t_R^p and t_R^o, respectively. At the moments of t_R^p and t_R^o, the $CWTC(t_{ij}^R(x,y))$ values obtained are comparatively small. Based on this, the distribution of $CWTC(t_{ij}^R(x,y))$ in the detection area can be obtained. Fusing the $CWTC(t_{ij}^R(x,y))$ distributions of multiple actuator-sensor pairs, the damage probability distribution $P(x,y)$ of the detection area is obtained as

$$P(x,y)=\frac{1}{N}\sum_{i=1}^{N-1}\sum_{j=i+1}^{N}CWTC(t_{ij}^R(x,y)), \tag{3}$$

where N is the total number of actuator-sensor pairs.

 doi:10.20944/preprints202404.1308.v1

2.2. ORAPID Algorithm

The ORAPID algorithm, similar to the DaS algorithm, also discretizes the detection area into regular grid nodes. However, unlike the DaS algorithm, the ORAPID algorithm does not require prior knowledge of the wave velocities and scattered waves' ToF. It reconstructs the probability distribution of the damaged image through the correlation between the damage signal and the baseline signal. The damage existing in the actuator-sensor path will affect the propagation characteristics of the Lamb waves, and the degree of Lamb waves affected by damage will gradually decrease as the distance of the actuator-damage-sensor propagation path increases. The correlation between the damage signal and the baseline signal is the signal correlation coefficient (*SCC*), which is expressed as

$$SCC = \frac{\sum_{k=1}^{M}(S_D(t)_k - \mu_{S_D(t)})(S_B(t)_k - \mu_{S_B(t)})}{\sqrt{\sum_{k=1}^{M}(S_D(t)_k - \mu_{S_D(t)})^2}\sqrt{\sum_{k=1}^{M}(S_B(t)_k - \mu_{S_B(t)})^2}}, \tag{4}$$

where $S_D(t)$ and $S_B(t)$ are the damage signal and baseline signal, respectively. $\mu_{S_D(t)}$ and $\mu_{S_B(t)}$ are the mean values of the damage signal and baseline signal, respectively. M is the length of the signal sequence. If there is no damage on the actuator-sensor propagation path, the two signals are identical, resulting in an *SCC* value of 1.0. If the phases of the two signals are opposite, the *SCC* is close to 0.

In the ORAPID algorithm, the signal difference coefficient (*SDC*) is defined as

$$SDC_{ij} = 1 - SCC_{ij}, \tag{5}$$

where the subscript *ij* represents the path formed by combining the *i* th actuator and the *j* th sensor. The *SDC* values of all actuator-sensor paths obtained are spatially distributed in an elliptical pattern to generate an *SDC* value image. The two focuses of the ellipse are located at the coordinates of the corresponding positions of the actuator and the sensor, as shown in Figure 3. The elliptic distribution function is defined as

$$\begin{cases} S_{ij}(x,y) = \dfrac{\lambda - R_{ij}(x,y)}{\lambda - 1}, & for\ \lambda > R_{ij}(x,y) \\ S_{ij}(x,y) = 0, & otherwise \end{cases}, \tag{6}$$

where the parameter λ is a shape factor that controls the size of the elliptical distribution, and the value of λ is greater than 1.0. $R_{ij}(x,y)$ is the ratio of the sum of the distance from the point $R(x,y)$ to the *i* th actuator and the *j* th sensor to the distance between the *i* th actuator and the *j* th sensor, which is defined as

$$R_{ij}(x,y) = \frac{\sqrt{(x-x_i)^2 + (y-y_i)^2} + \sqrt{(x-x_j)^2 + (y-y_j)^2}}{\sqrt{(x_i-x_j)^2 + (y_i-y_j)^2}}, \tag{7}$$

where (x, y) are the coordinates of any position in the detection area. $A(x_i, y_i)$ is the position coordinate of the *i* th actuator, and $S(x_j, y_j)$ is the position coordinate of the *j* th sensor.

 doi:10.20944/preprints202404.1308.v1

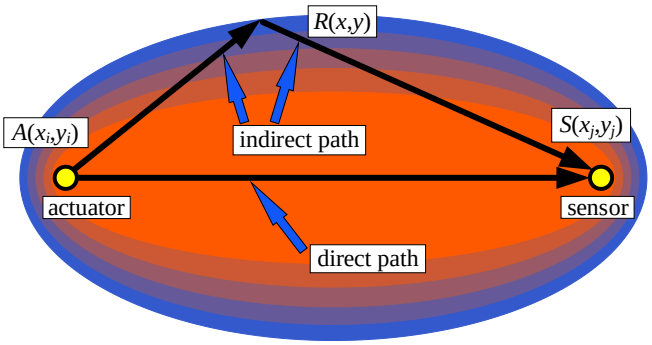

Figure 3. The ellipse distribution diagram of the ORAPID algorithm.

The product of the *SDC* value of each actuator-sensor pair and the elliptic distribution function $S_{ij}(x,y)$ value is linearly superimposed to obtain a normalized damage probability distribution $P(x,y)$, which is defined as

$$P(x,y)=\sum_{i=1}^{N-1}\sum_{j=i+1}^{N} SDC_{ij}S_{ij}(x,y), \tag{8}$$

where N is the total number of actuator-sensor pairs.

2.3. IRAPID algorithm

Considering that the *SCC* is not necessarily linearly related to the distance of the actuator-damage-sensor propagation path, this paper proposes an IRAPID algorithm. Replace the SDC with the signal ratio coefficient (*SRC*), and *SRC* is defined as

$$SRC_{ij}=1/SCC_{ij}, \tag{9}$$

where the subscript *ij* represents the path formed by combining the *i* th actuator and the *j* th sensor.

The corresponding damage probability distribution $P(x,y)$ is defined as

$$P(x,y)=\sum_{i=1}^{N-1}\sum_{j=i+1}^{N} SRC_{ij}S_{ij}(x,y), \tag{10}$$

where N is the total number of actuator-sensor pairs.

3. Experiment

3.1. Preparation of CFRP Bending Plate

The mold for preparing CFRP bending plates is shown in Figure 4. The material used in the mold is aluminum. The CFRP bending plate uses resin as the matrix and T300-12K-200g-42% unidirectional carbon fiber as the reinforcing material. The preparation environment was −10 atmospheric pressure. The layup sequence for the CFRP bending plate is $[0°/90°/45°/–45°/90°/0°]_s$. The geometric dimensions of the CFRP bending plate and the configuration of the PZT are shown in Figure 5. The coordinate position of PZT numbered P4 is set as the coordinate origin, the coordinate of PZT numbered P1 is (0 mm, 200 mm), the coordinate of PZT numbered P2 is (200 mm, 200 mm), and the coordinate of PZT numbered P3 is (200 mm, 0 mm). The straight edge direction of the CFRP bending plate is the X-axis, and the circumferential direction of the bending edge of the CFRP bending plate is the Y-axis. The thickness of the CFRP bending plate is 2.28 mm, the side length in the X-axis and Y-axis directions is 600 mm, the bending radius R=30 mm, and the bending angle is 90°. Delamination damage was simulated by filling the anti-sticking paper in the middle layer of the CFRP bending plate, which was located at the center of the CFRP bending plate with coordinates (x, y) = (100 mm, 100 mm). Three

 doi:10.20944/preprints202404.1308.v1

CFRP bending plates, including a healthy bending plate and two bending plates with delamination damage sizes of Φ20 mm and Φ40 mm, were prepared for experimental research, respectively.

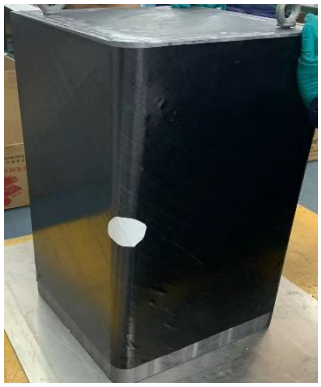

Figure 4. Aluminum molds.

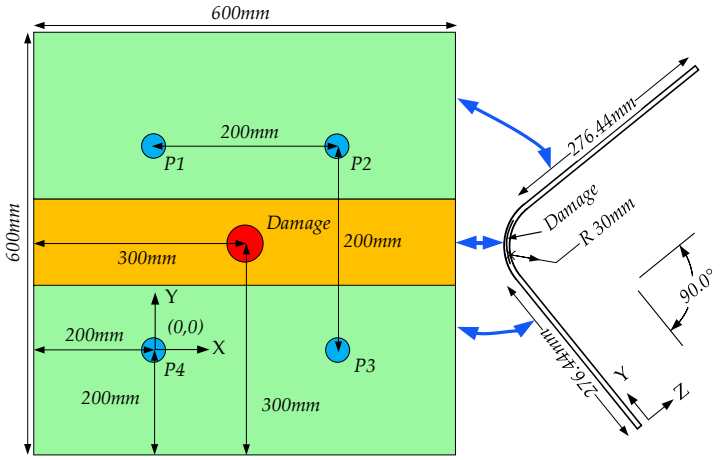

Figure 5. CFRP bending plate geometric dimension and PZT configuration.

3.2. Experimental Procedure

The experimental system is shown in Figure 6. The PC controls the arbitrary wave function generator (AFG−31000) through the software ArbExpress to generate a 5-cycle narrowband Tone-Burst signal modulated by the Hanning window, with a signal voltage amplitude of 10 Vpp. The excitation signal is defined as

$$V(t) = 0.5(1 - \cos(2\pi ft / 5))\sin(2\pi ft)\,, \tag{11}$$

where t is the time, and the excitation frequency f varies from 220 kHz to 320 kHz in a step of 10 kHz.

In the experiment, honey was used as the couplant to paste the PZT transducer onto the CFRP bending plate, and the PZT transducer was fixed to the CFRP bending plate with insulating tape. The excitation signal was amplified three times by the power amplifier (ATA−4011), and then a PZT transducer was excited to generate Lamb waves in the CFRP bending plate. Other PZT transducers were used to receive the Lamb wave signals. The received Lamb wave signals were amplified by a preamplifier (OLYMPUS−5682) and then saved by an oscilloscope with a sampling rate of 250 MS/s. Throughout the experiment, the Lamb wave signals for each detection condition were gathered on 16 occasions and averaged to mitigate the influence of noise interference. The gathered Lamb wave signals were processed according to the signal processing method in Section 2.

Preprints.org (www.preprints.org) | NOT PEER-REVIEWED | Posted: 22 April 2024 doi:10.20944/preprints202404.1308.v1

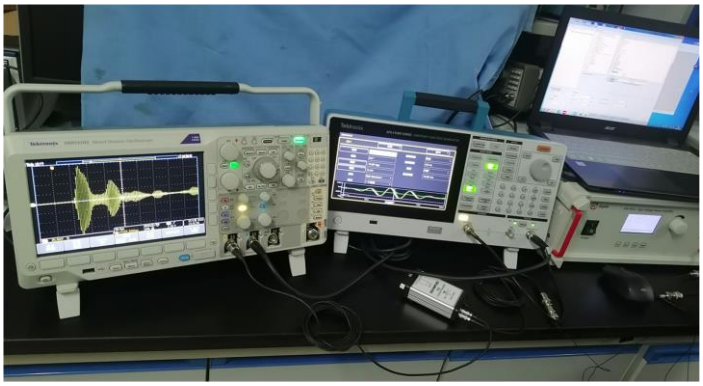

Figure 6. The experimental system.

4. Results and Discussion

4.1. DaS Algorithm Localization Results

The DaS algorithm requires the Lamb wave group velocity as prior knowledge. The Lamb wave group velocity of the CFRP obtained by theoretical calculation differs from that of the CFRP under actual situations. The equation for calculating the Lamb wave group velocity is defined as

$$V = \frac{D}{ToF}, \tag{12}$$

where D is the distance between the actuator and the sensor. To obtain ToF, the *CWT* was applied to both the excitation and baseline signal. In Equation (12), ToF represents the time elapsed from the peak of the excitation signal's *CWT* to the first peak of the baseline signal's *CWT*. Figure 7a shows the baseline signal of path P1-P2 at a frequency of 220 kHz, with D=200 mm. Figure 7b shows the *CWT* of the baseline signal and excitation signal. The group velocities of Lamb waves at various frequencies are shown in Table 1.

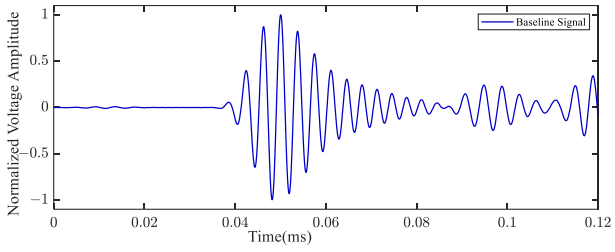

(a)

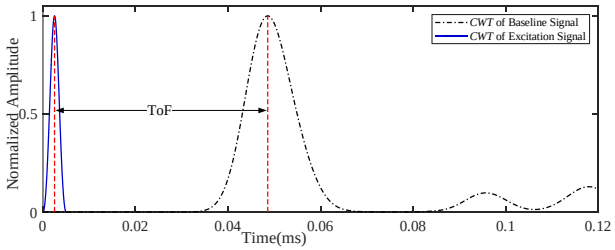

(b)

Figure 7. The baseline signal and its *CWT* of the P1−P2 path at a frequency of 220 kHz: (**a**) baseline signal; (**b**) the *CWT* of baseline signal and excitation signal.

Table 1. The group velocities of Lamb waves at various frequencies.

Preprints.org (www.preprints.org) | NOT PEER-REVIEWED | Posted: 22 April 2024 doi:10.20944/preprints202404.1308.v1

f (kHz)	220	230	240	250	260	270	280	290	300	310	320
V (m/s)	5263.9	5035.3	4915.5	4667.3	4569.4	4343.0	4280.0	4148.6	4122.1	4067.5	4058.7

At the frequencies of 220 kHz, 270 kHz, and 320 kHz, the Lamb wave signals of the P1−P2 path are shown in Figure 8. The direct Lamb wave of the P1−P2 path did not propagate through the delamination damage and bending structure. As can be seen from Figure 8, the amplitude and phase of the Lamb wave signal change due to the existence of delamination damage, and the influence of Φ40 mm delamination damage on the Lamb wave signal is more obvious than that of Φ20 mm delamination damage. In addition, with the increase in frequency, the impact of delamination damage on Lamb wave signals becomes more significant.

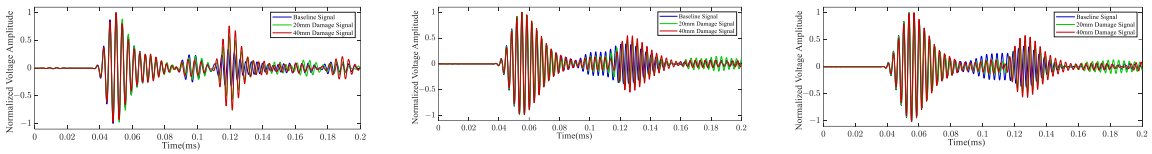

(a) **(b)** **(c)**

Figure 8. The Lamb wave signals at various frequencies of the P1-P2 path: (**a**) 220 kHz; (**b**) 270 kHz; (**c**) 320 kHz.

At the frequency of 320 kHz, the Lamb wave signal of the P2−P3 path and P2−P4 path are shown in Figure 9. The direct Lamb wave of the P2−P3 path propagates through the bending structure, and the direct Lamb wave of the P2−P4 path propagates through the delamination damage and the bending structure. As can be seen from Figure 9a, the energy distribution of the Lamb wave in the time domain is altered due to the existence of delamination damage. Similarly, the energy value of the Lamb wave is altered due to the existence of delamination damage, as illustrated in Figure 9b. Moreover, the change in energy caused by Φ40mm delamination damage is greater than that caused by Φ20mm delamination damage. It can be concluded that the Lamb wave signal is affected differently by delamination damage under various frequencies and propagation paths.

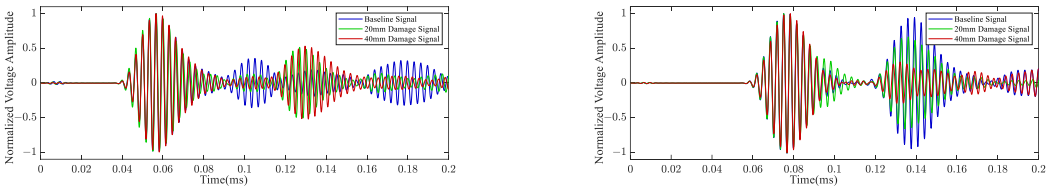

(a) **(b)**

Figure 9. The Lamb wave signal of different paths under a frequency of 320 kHz: (**a**) P2−P3 path; (**b**) P2−P4 path.

For the case where the delamination damage size is Φ20 mm, the scattered wave signals of the P1−P2 path at frequencies of 220 kHz, 270 kHz, and 320 kHz are shown in Figure 10. The *CWTC* was obtained by processing the scattered wave signal with *CWT*, and *CWTC* is shown in Figure 11. At the frequency of 320 kHz, the scattered wave signals of Φ20 mm delamination damage under different paths are shown in Figure 12, and the *CWTC* of them are shown in Figure 13. As can be seen from Figures 10–13, by utilizing the *CWT* to process the scattered wave signals, we can accurately obtain their time-frequency information, which is beneficial to the localization of delamination damage.

 doi:10.20944/preprints202404.1308.v1

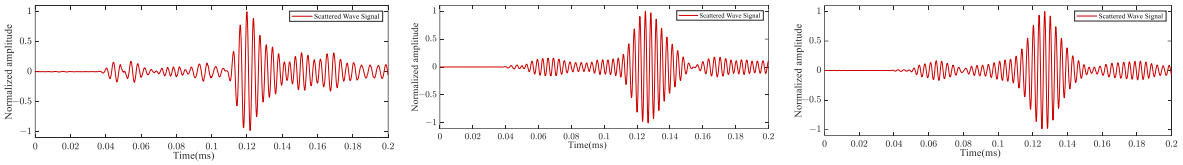

(a) (b) (c)

Figure 10. The scattered wave signals of Φ20 mm delamination damage under the P1-P2 path: (**a**) 220 kHz; (**b**) 270 kHz; (**c**) 320 kHz.

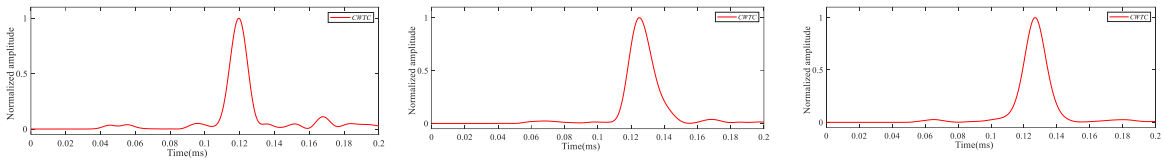

(a) (b) (c)

Figure 11. The *CWTC* of Φ20 mm delamination damage under the P1-P2 path: (**a**) 220 kHz; (**b**) 270 kHz; (**c**) 320 kHz.

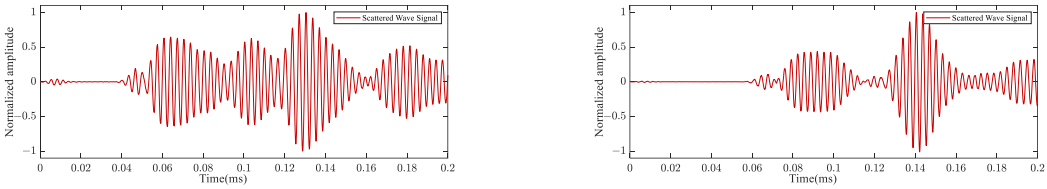

(a) (b)

Figure 12. The scattered wave signals of Φ20 mm delamination damage under the frequency of 320 kHz: (**a**) P2−P3 path; (**b**) P2−P4 path.

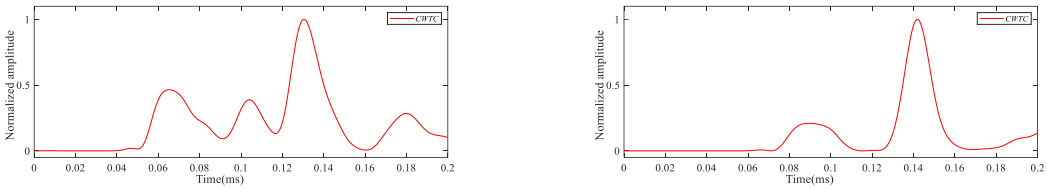

(a) (b)

Figure 13. The *CWTC* of Φ20 mm delamination damage under the frequency of 320 kHz: (**a**) P2−P3 path; (**b**) P2−P4 path.

For the case where the delamination damage size is Φ40 mm, the scattered wave signals of the P1−P2 path at frequencies of 220 kHz, 270 kHz, and 320 kHz are shown in Figure 14, and the *CWTC* of them are shown in Figure 15. At the frequency of 320 kHz, the scattered wave signals of Φ40 mm delamination damage under different paths are shown in Figure 16, and the *CWTC* of them are shown in Figure 17. As can be seen from Figures 10–17, the scattered wave signals of the P2-P3 and P2-P4 paths are more complex in waveform than those on the P1-P2 path. This may be due to the scattering of Lamb waves during their propagation in CFRP, which was caused by the existence of bending structures and delamination damage.

Preprints.org (www.preprints.org) | NOT PEER-REVIEWED | Posted: 22 April 2024 doi:10.20944/preprints202404.1308.v1

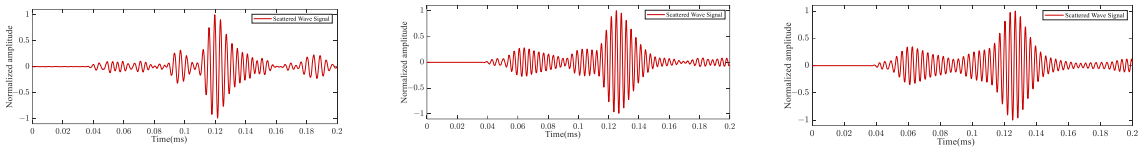

(a) (b) (c)

Figure 14. The scattered wave signals of Φ40 mm delamination damage under the P1-P2 path: (**a**) 220 kHz; (**b**) 270 kHz; (**c**) 320 kHz.

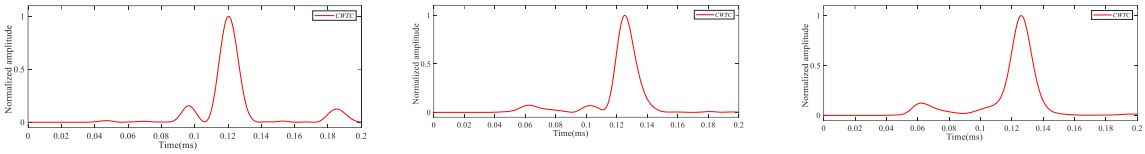

(a) (b) (c)

Figure 15. The *CWTC* of Φ40 mm delamination damage under the P1-P2 path: (**a**) 220 kHz; (**b**) 270 kHz; (**c**) 320 kHz.

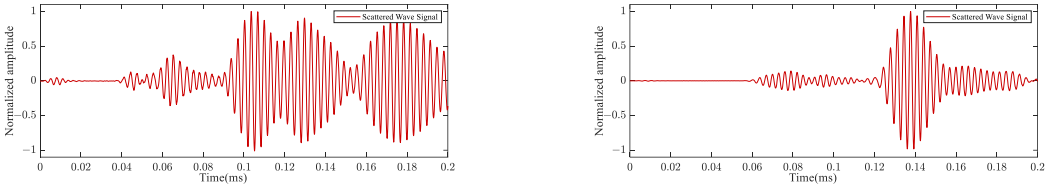

(a) (b)

Figure 16. The scattered wave signals of Φ40 mm delamination damage under the frequency of 320 kHz: (**a**) P2−P3 path; (**b**) P2−P4 path.

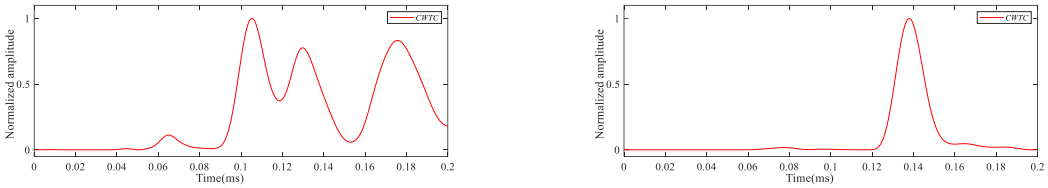

(a) (b)

Figure 17. The *CWTC* of Φ40 mm delamination damage under the frequency of 320 kHz: (**a**) P2−P3 path; (**b**) P2−P4 path.

According to the *CWTC* obtained from the scattered wave signal of the delamination damage, the DaS algorithm was used to locate the delamination damage, and the delamination damage localization imaging results can be obtained. The localization imaging results of the Φ20 mm delamination damage by the DaS algorithm are shown in Figure 18. With a set threshold, the localization imaging results of the Φ20 mm delamination damage by the DaS algorithm are shown in Figure 19. The localization imaging results of the Φ40 mm delamination damage by the DaS algorithm and the localization imaging results under the set threshold are shown in Figures 20 and 21, respectively. The localization imaging results of the DaS algorithm for the X and Y axes are shown in Table 2, where f_m represents the frequency-averaged of the localization imaging results. As can be seen from the figures, more accurate delamination damage localization results can be obtained with higher-frequency Lamb waves. The frequency-averaged localization imaging results of delamination

Preprints.org (www.preprints.org) | NOT PEER-REVIEWED | Posted: 22 April 2024 doi:10.20944/preprints202404.1308.v1

damage were obtained by superimposing and averaging the delamination damage localization results at all frequencies. The frequency-averaged localization imaging results of Φ20 mm delamination damage by the DaS algorithm are shown in Figure 22, and the frequency-averaged localization imaging results of Φ40 mm delamination damage are shown in Figure 23. From the frequency-averaged localization imaging results, it can be seen that by superimposing and averaging the delamination damage localization results at all frequencies, the errors in the localization of delamination damage at some frequencies can be eliminated, and the reliability of delamination damage localization can be improved.

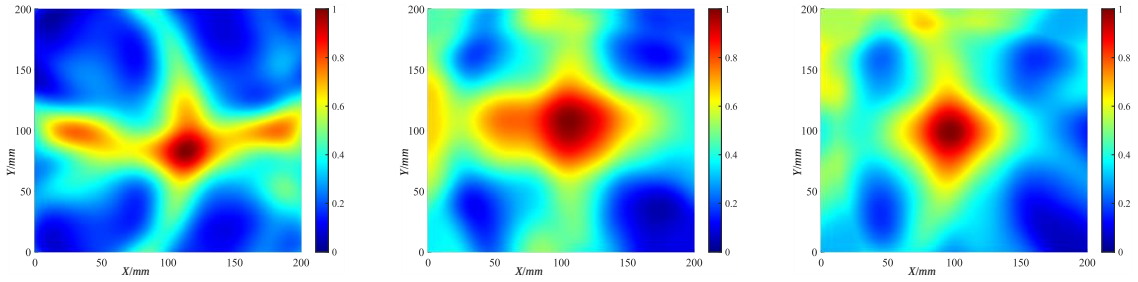

(a) **(b)** **(c)**

Figure 18. The localization imaging results of the Φ20 mm delamination damage by the DaS algorithm: (**a**) 220 kHz; (**b**) 270 kHz; (**c**) 320 kHz.

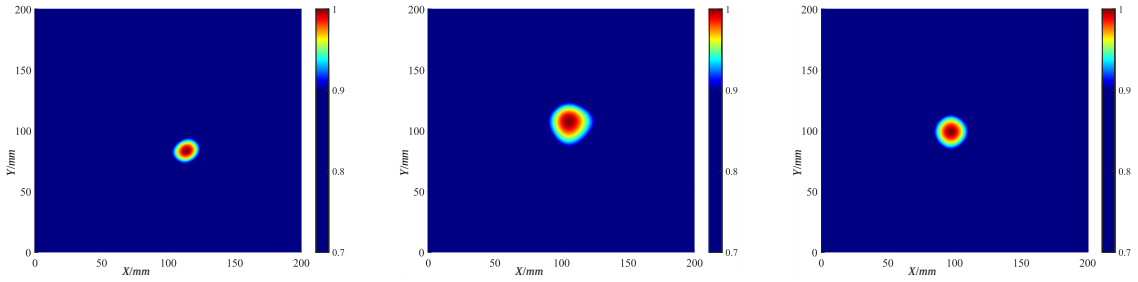

(a) **(b)** **(c)**

Figure 19. The localization imaging results of the Φ20 mm delamination damage by the DaS algorithm under a threshold setting: (**a**) 220 kHz; (**b**) 270 kHz; (**c**) 320 kHz.

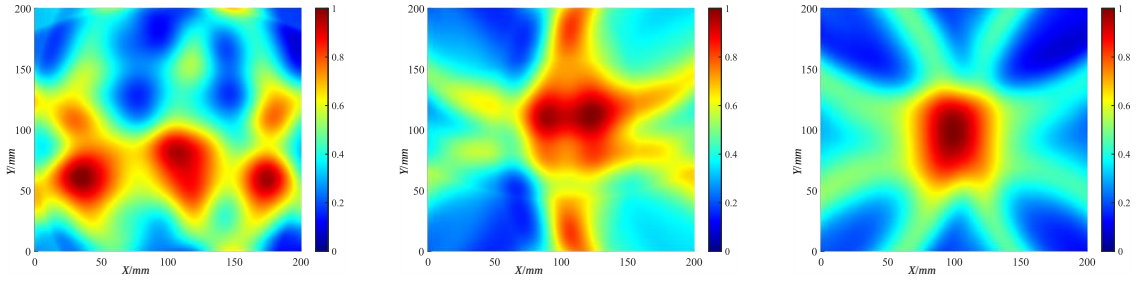

(a) **(b)** **(c)**

Figure 20. The localization imaging results of the Φ40 mm delamination damage by the DaS algorithm: (**a**) 220 kHz; (**b**) 270 kHz; (**c**) 320 kHz.

Preprints.org (www.preprints.org) | NOT PEER-REVIEWED | Posted: 22 April 2024 doi:10.20944/preprints202404.1308.v1

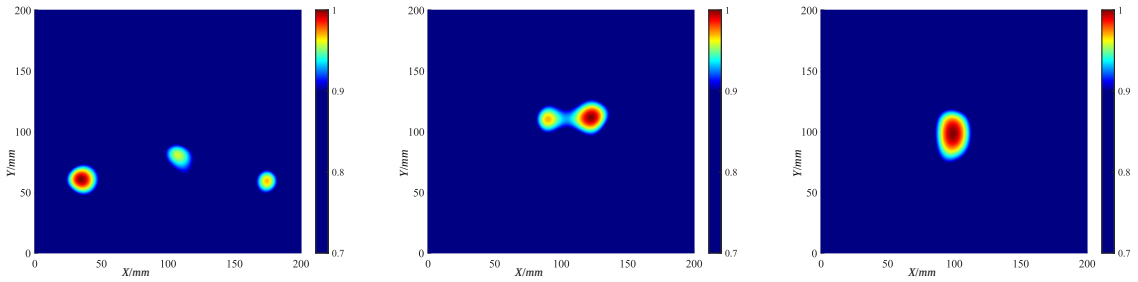

(a) (b) (c)

Figure 21. The localization imaging results of the Φ40 mm delamination damage by the DaS algorithm under a threshold setting: (**a**) 220 kHz; (**b**) 270 kHz; (**c**) 320 kHz.

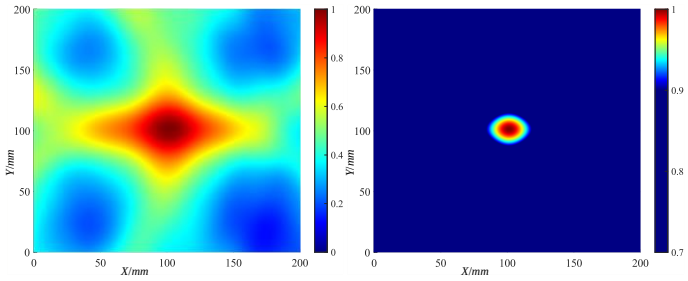

(a) (b)

Figure 22. The frequency-averaged localization imaging results of the Φ20 mm delamination damage by the DaS algorithm: (**a**) frequency-averaged localization imaging results; (**b**) frequency-averaged localization imaging results with a threshold.

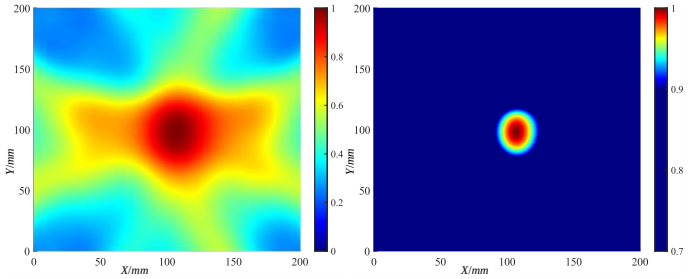

(a) (b)

Figure 23. The frequency-averaged localization imaging results of the Φ40 mm delamination damage by the DaS algorithm: (**a**) frequency-averaged localization imaging results; (**b**) frequency-averaged localization imaging results with a threshold.

Table 2. The localization imaging results of the X and Y axes by the DaS algorithm.

	f **(kHz)**	220	230	240	250	260	270	280	290	300	310	320	f_m
X	Φ20(mm)	107.4	99.4	91.8	88.8	108.6	105.8	105.0	99.2	96.6	94.2	93.8	98.6
	Φ40(mm)	106.0	165.0	161.0	148.0	138.6	122.4	109.6	104.0	103.0	100.8	99.2	106.6
Y	Φ20(mm)	95.2	102.0	100.8	101.8	113.2	108.0	105.8	101.2	100.0	97.4	98.4	101.0
	Φ40(mm)	87.2	106.8	105.2	104.4	105.0	111.6	114.2	88.2	89.8	95.6	98.4	98.4

4.2. ORAPID Algorithm Localization Results

According to the obtained Lamb wave signal, the *SCC* of the damage signal and the baseline signal was calculated by equation (4), and the ORAPID algorithm and IRAPID algorithm were used to locate the delamination damage respectively. The localization imaging results of the Φ20 mm

 doi:10.20944/preprints202404.1308.v1

delamination damage by the ORAPID algorithm are shown in Figure 24. With a set threshold, the localization imaging results of the Φ20 mm delamination damage by the ORAPID algorithm are shown in Figure 25. The localization imaging results of the Φ40 mm delamination damage by the ORAPID algorithm and the localization imaging results under the set threshold are shown in Figures 26 and 27, respectively. The localization imaging results of the ORAPID algorithm for the X and Y axes are shown in Table 3.

It can be seen from the figure that the use of higher frequency Lamb waves for detection can obtain more accurate delamination damage localization results. The localization imaging results of the Φ20 mm delamination damage by the ORAPID algorithm are superior to those of the Φ40 mm delamination damage by the same algorithm.

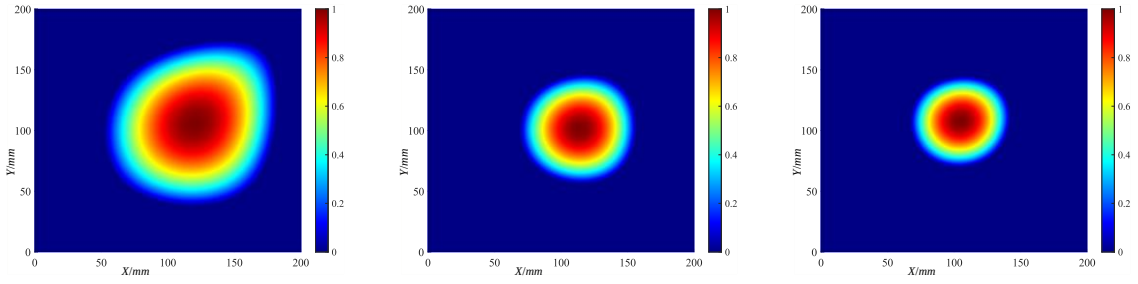

(a) **(b)** **(c)**

Figure 24. The localization imaging results of the Φ20 mm delamination damage by the ORAPID algorithm: (**a**) 220 kHz; (**b**) 270 kHz; (**c**) 320 kHz.

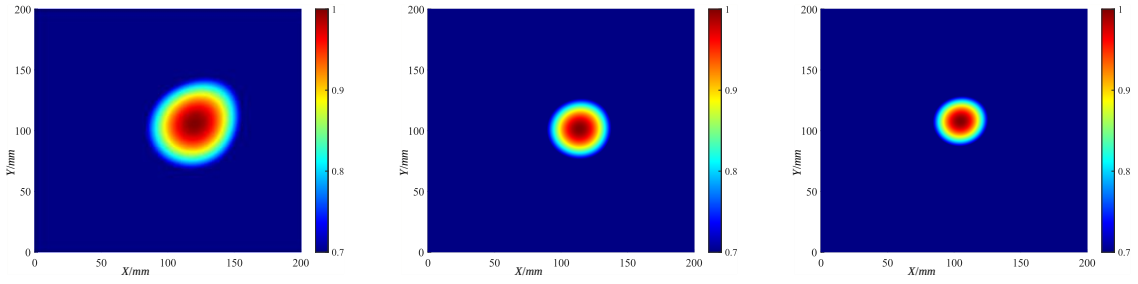

(a) **(b)** **(c)**

Figure 25. The localization imaging results of the Φ20 mm delamination damage by the ORAPID algorithm under a threshold setting: (**a**) 220 kHz; (**b**) 270 kHz; (**c**) 320 kHz.

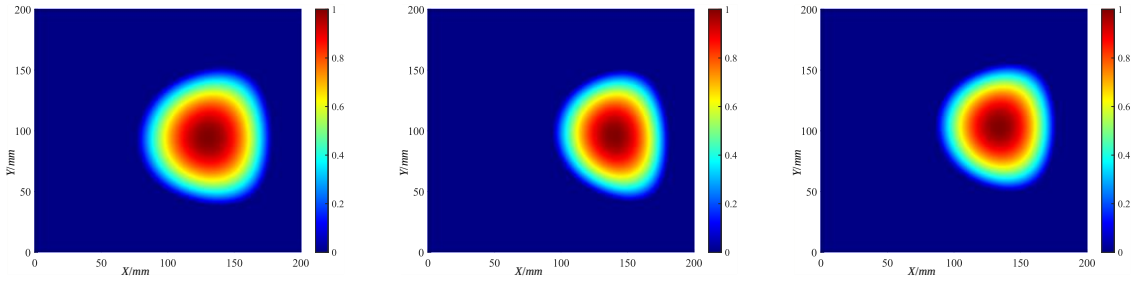

(a) **(b)** **(c)**

Figure 26. The localization imaging results of the Φ40 mm delamination damage by the ORAPID algorithm: (**a**) 220 kHz; (**b**) 270 kHz; (**c**) 320 kHz.

Preprints.org (www.preprints.org) | NOT PEER-REVIEWED | Posted: 22 April 2024 doi:10.20944/preprints202404.1308.v1

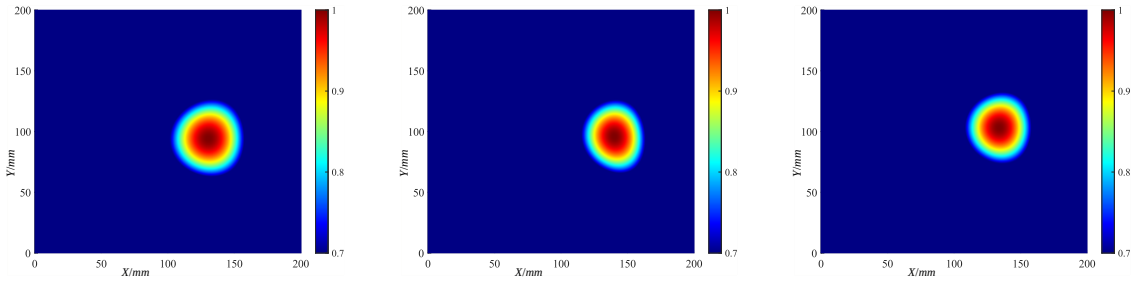

(a) **(b)** **(c)**

Figure 27. The localization imaging results of the Φ40 mm delamination damage by the ORAPID algorithm under a threshold setting: (**a**) 220 kHz; (**b**) 270 kHz; (**c**) 320 kHz.

Table 3. The localization imaging results of the X and Y axes by the ORAPID algorithm.

	f (kHz)	220	230	240	250	260	270	280	290	300	310	320	f_m
X	Φ20(mm)	120.0	118.1	118.0	116.7	116.5	113.9	112.7	110.8	108.9	106.8	104.8	112.2
	Φ40(mm)	130.2	130.1	133.6	136.2	138.7	139.9	137.7	136.8	136.0	135.0	133.8	135.3
Y	Φ20(mm)	106.0	99.7	98.0	96.7	98.7	101.5	103.2	104.7	106.0	107.1	107.9	103.2
	Φ40(mm)	94.5	97.1	96.5	96.7	95.4	96.0	97.6	99.1	100.4	101.8	103.3	98.1

The delamination damage localization results at all frequencies were superimposed and averaged to obtain the frequency-averaged localization imaging results of delamination damage. The frequency-average localization imaging results of Φ20 mm and Φ40 mm delamination damage by the ORAPID algorithm are shown in Figures 28 and 29, respectively. It can be seen from the frequency-averaged localization imaging results that the superimposing and averaging of the localization results at all frequencies does not significantly improve the accuracy of delamination damage localization.

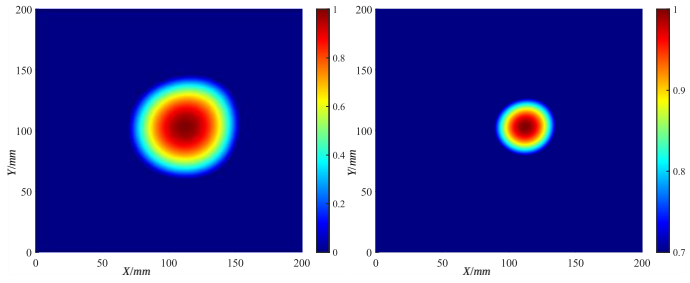

(a) **(b)**

Figure 28. The frequency-averaged localization imaging results of the Φ20 mm delamination damage by the ORAPID algorithm: (**a**) frequency-averaged localization imaging results; (**b**) frequency-averaged localization imaging results with a threshold.

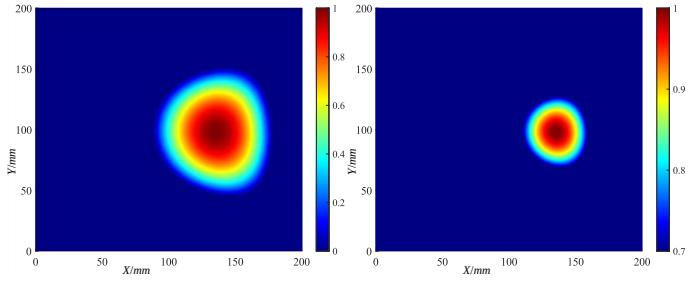

(a) **(b)**

 doi:10.20944/preprints202404.1308.v1

Figure 29. The frequency-averaged localization imaging results of the Φ40 mm delamination damage by the ORAPID algorithm: (**a**) frequency-averaged localization imaging results; (**b**) frequency-averaged localization imaging results with a threshold.

4.3. IRAPID Algorithm Localization Results

The localization imaging results of the Φ20 mm delamination damage by the IRAPID algorithm are shown in Figure 30. With a set threshold, the localization imaging results of the Φ20 mm delamination damage by the IRAPID algorithm are shown in Figure 31. The localization imaging results of the Φ40 mm delamination damage by the IRAPID algorithm and the localization imaging results under the set threshold are shown in Figures 32 and 33, respectively. The localization imaging results of the IRAPID algorithm for the X and Y axes are shown in Table 4.

It is evident from the localization imaging results that there is a weak correlation between the delamination damage localization results and frequency. The localization imaging results of the Φ20 mm delamination damage by the IRAPID algorithm are more accurate than that of the Φ40 mm delamination damage.

The frequency-average localization imaging results of Φ20 mm and Φ40 mm delamination damage by the IRAPID algorithm are shown in Figures 34 and 35, respectively. It can be seen from the frequency-averaged localization imaging results that, similar to the ORAPID algorithm, the IRAPID algorithm does not significantly improve the accuracy of delamination damage localization by superimposing and averaging the localization results at all frequencies.

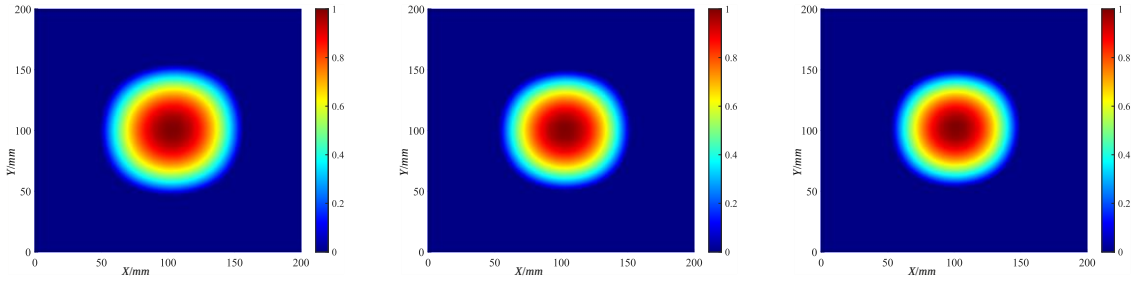

(a) **(b)** **(c)**

Figure 30. The localization imaging results of the Φ20 mm delamination damage by the IRAPID algorithm: (**a**) 220 kHz; (**b**) 270 kHz; (**c**) 320 kHz.

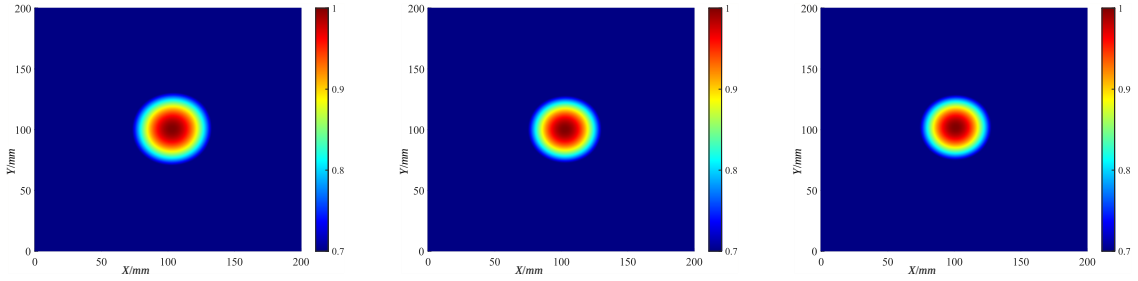

(a) **(b)** **(c)**

Figure 31. The localization imaging results of the Φ20 mm delamination damage by the IRAPID algorithm under a threshold setting: (**a**) 220 kHz; (**b**) 270 kHz; (**c**) 320 kHz.

Preprints.org (www.preprints.org) | NOT PEER-REVIEWED | Posted: 22 April 2024 doi:10.20944/preprints202404.1308.v1

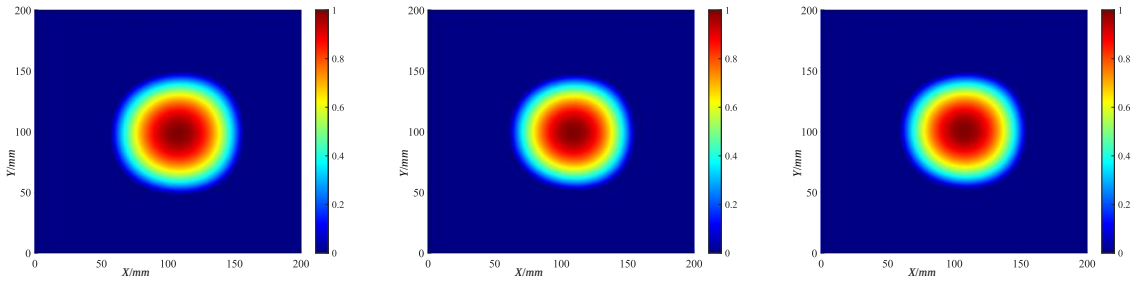

(a) **(b)** **(c)**

Figure 32. The localization imaging results of the Φ40 mm delamination damage by the IRAPID algorithm: (**a**) 220 kHz; (**b**) 270 kHz; (**c**) 320 kHz.

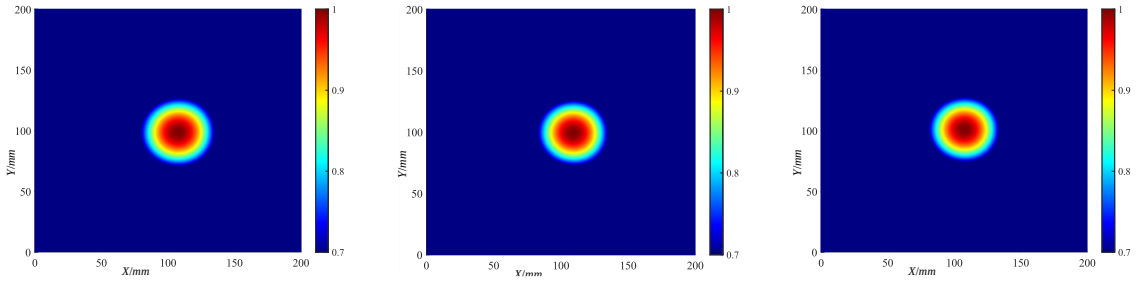

(a) **(b)** **(c)**

Figure 33. The localization imaging results of the Φ40 mm delamination damage by the IRAPID algorithm under a threshold setting: (**a**) 220 kHz; (**b**) 270 kHz; (**c**) 320 kHz.

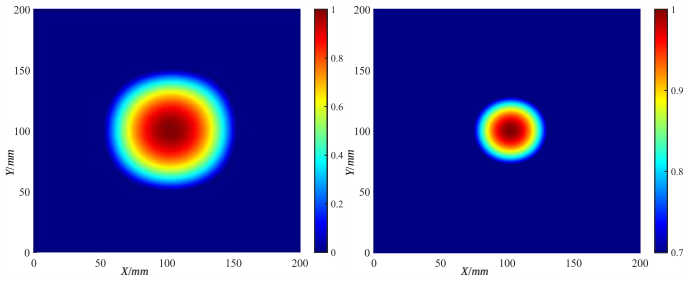

(a) **(b)**

Figure 34. The frequency-averaged localization imaging results of the Φ20 mm delamination damage by the IRAPID algorithm: (**a**) frequency-averaged localization imaging results; (**b**) frequency-averaged localization imaging results with a threshold.

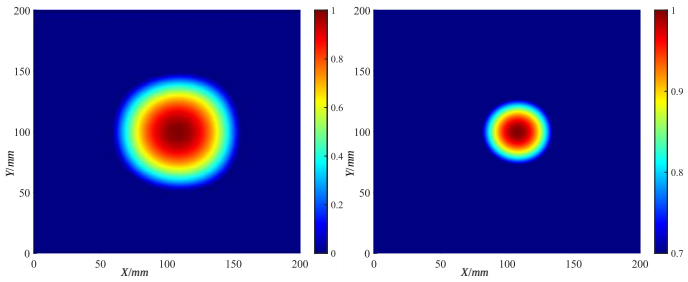

(a) **(b)**

Figure 35. The frequency-averaged localization imaging results of the Φ40 mm delamination damage by the IRAPID algorithm: (**a**) frequency-averaged localization imaging results; (**b**) frequency-averaged localization imaging results with a threshold.

Preprints.org (www.preprints.org) | NOT PEER-REVIEWED | Posted: 22 April 2024 doi:10.20944/preprints202404.1308.v1

Table 4. The localization imaging results of the X and Y axes by the IRAPID algorithm.

	f (kHz)	220	230	240	250	260	270	280	290	300	310	320	f_m
X	Φ20(mm)	103.0	102.9	103.2	103.1	103.3	102.9	102.7	102.4	102.0	101.6	101.1	102.5
	Φ40(mm)	107.4	106.5	107.0	107.8	108.5	109.0	108.3	108.2	108.1	107.9	107.6	107.9
Y	Φ20(mm)	100.6	99.8	99.6	99.3	99.7	100.3	100.6	101.0	101.3	101.7	101.9	100.6
	Φ40(mm)	98.7	99.6	99.6	99.5	99.3	99.5	99.7	100.0	100.3	100.6	101.0	99.8

At each frequency, the results of every algorithm for Φ20 mm and Φ40 mm delamination damage localization are shown in Figures 36 and 37, respectively. It can be seen from the figure that with the change of frequency, the DaS algorithm and the ORAPID algorithm exhibit significant fluctuation in their accuracy of delamination damage localization, and the IRAPID algorithm shows better stability in the delamination damage localization. The IRAPID algorithm outperforms the DaS and the ORAPID algorithm in delamination damage localization within the frequency range under consideration. The IRAPID algorithm can achieve satisfactory results for the delamination damage localization at various frequencies.

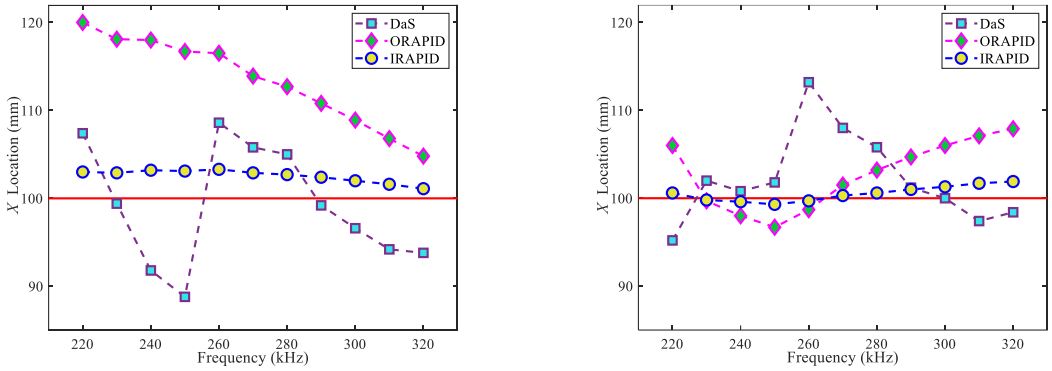

(a) **(b)**

Figure 36. Φ20 mm delamination damage localization results: (**a**) X-axis localization results; (**b**) Y-axis localization results (the red horizontal line represents the real delamination damage localization).

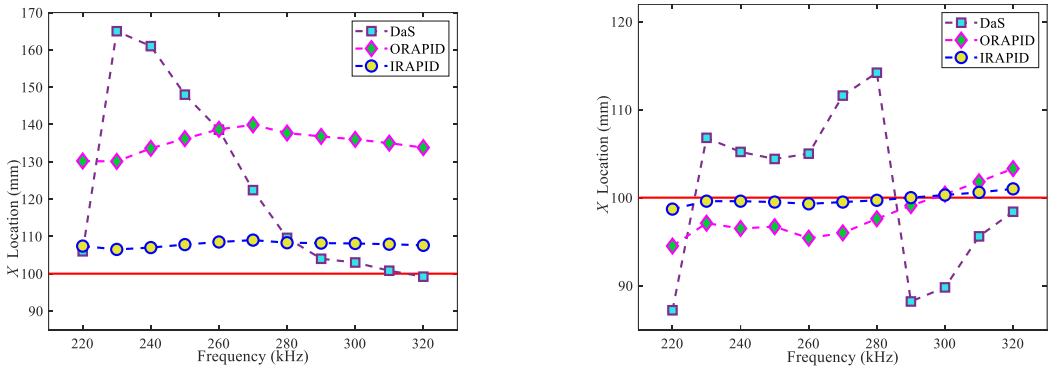

(a) **(b)**

Figure 37. Φ40 mm delamination damage localization results: (**a**) X-axis localization results; (**b**) Y-axis localization results (the red horizontal line represents the real delamination damage localization).

The localization errors of every algorithm for the Φ20 mm and Φ40 mm delamination damage are shown in Tables 5 and 6, respectively. It can be found from Tables 5 and 6 that, when the frequency-averaged localization results were used as the evaluation criterion, the localization error of the IRAPID algorithm for delamination damage was significantly lower than that of the DaS algorithm and the original RAPID algorithm. The localization accuracy of each algorithm for

 doi:10.20944/preprints202404.1308.v1

delamination damage in the X-axis direction is lower than that in the Y-axis direction. This may be due to the delamination damage at the CFRP bending structure, and the bending structure is along the X-axis direction. The bending structure aggravates the complexity of the Lamb wave signal and increases the localization error in the X-axis direction.

Table 5. The localization error of Φ20 mm delamination damage.

f (kHz)		220	230	240	250	260	270	280	290	300	310	320	f_m
DaS	X(mm)	7.4	0.6	8.2	11.2	8.6	5.8	5.0	0.8	3.4	5.8	6.2	5.7
	Y(mm)	4.8	2.0	0.8	1.8	13.2	8.0	5.8	1.2	0	2.6	1.6	3.8
ORAPID	X(mm)	20.0	18.1	18.0	16.7	16.5	13.9	12.7	10.8	8.9	6.8	4.8	13.4
	Y(mm)	6.0	0.3	2.0	3.3	1.3	1.5	3.2	4.7	6.0	7.1	7.9	3.9
IRAPID	X(mm)	3.0	2.9	3.2	3.1	3.3	2.9	2.7	2.4	2.0	1.6	1.1	2.6
	Y(mm)	0.6	0.2	0.4	0.7	0.3	0.3	0.6	1.0	1.3	1.7	1.9	0.8

Table 6. The localization error of Φ40 mm delamination damage.

f (kHz)		220	230	240	250	260	270	280	290	300	310	320	f_m
DaS	X(mm)	6.0	65.0	61.0	48.0	38.6	22.4	9.6	4.0	3.0	0.8	0.8	23.6
	Y(mm)	12.8	6.8	5.2	4.4	5.0	11.6	14.2	11.8	10.2	4.4	1.6	8.0
ORAPID	X(mm)	30.2	30.1	33.6	36.2	38.7	39.9	37.7	36.8	36.0	35.0	33.8	35.3
	Y(mm)	5.5	2.9	3.5	3.3	4.6	4.0	2.4	0.9	0.4	1.8	3.3	3.0
IRAPID	X(mm)	7.4	6.5	7.0	7.8	8.5	9.0	8.3	8.2	8.1	7.9	7.6	7.8
	Y(mm)	1.3	0.4	0.4	0.5	0.7	0.5	0.3	0	0.3	0.6	1.0	0.5

The variation of the localization errors of the Φ20 mm and Φ40 mm delamination damage on the X-axis and Y-axis with frequency is shown in Figures 38 and 39, respectively. As can be seen from Figures 38 and 39, compared with the Φ40 mm delamination damage, the localization results of the Φ20 mm delamination damage are more accurate. In addition, the localization results of Φ40 mm delamination damage by each algorithm fluctuated greatly with the change in frequency. This may be due to the scattering of Lamb waves encountering the boundaries of delamination damage. As the size of delamination damage increases, the error in ToF obtained from scattered waves increases due to the increase in the boundary of delamination damage, ultimately making delamination damage localization increasingly challenging.

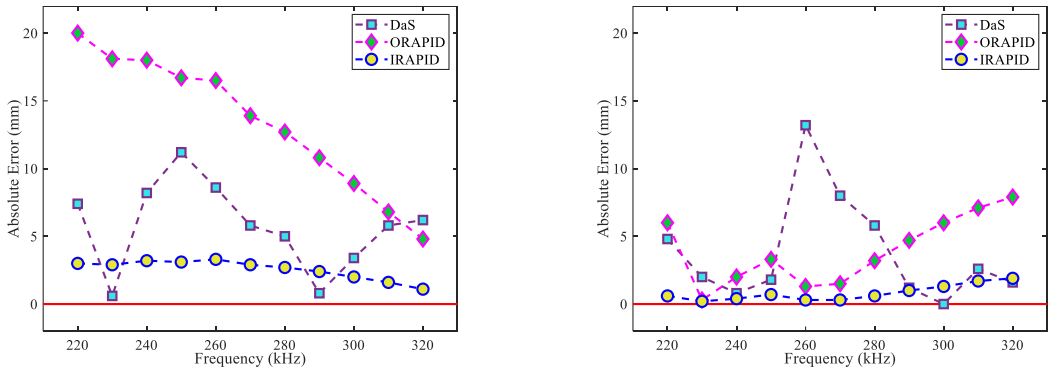

Figure 38. Φ20 mm delamination damage localization errors: (**a**) X-axis localization errors; (**b**) Y-axis localization errors (the red horizontal line represents the baseline of delamination damage localization error).

 doi:10.20944/preprints202404.1308.v1

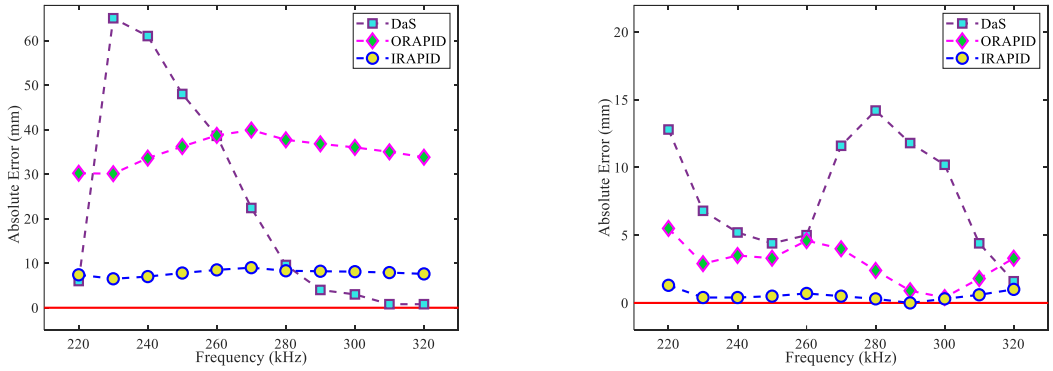

Figure 39. Φ40 mm delamination damage localization errors: (**a**) X-axis localization errors; (**b**) Y-axis localization errors (the red horizontal line represents the baseline of delamination damage localization error).

5. Conclusions

An ORAPID method was proposed in this paper to conduct experimental research on the delamination damage localization of CFRP bending plates using Lamb waves. In the experiment, three CFRP bending plates were prepared, including one healthy bending plate and two bending plates with delamination damage sizes of Φ20 mm and Φ40 mm, respectively. The conclusions are as follows:

(1) Compared with the DaS algorithm and the ORAPID algorithm, the IRAPID algorithm has achieved more accurate results in the localization of delamination damage at each frequency.
(2) In the range of frequency variation considered, the stability of the IRAPID algorithm for delamination damage localization is superior to that of the DaS algorithm and the ORAPID algorithm.
(3) The localization of delamination damage will become increasingly challenging due to the increase in its size.
(4) The accuracy of delamination damage localization in different axial directions will vary due to the existence of bending structures. The accuracy of delamination damage localization is higher in the Y-axis direction than in the X-axis direction.
(5) To a certain extent, it mitigates the potential localization errors associated with single-frequency detection by averaging the localization results across various frequencies. Lamb waves with multiple frequencies can be employed for delamination damage localization detection, and the detection results at each frequency are averaged to enhance the reliability of localization.

Author Contributions: Conceptualization, Q.Y. and S.Z.; methodology, Q.Y.; validation, Q.Y. and Y.C.; formal analysis, Q.Y. and S.Z.; investigation, Q.Y. and Y.C.; resources, S.Z.; data curation, Q.Y., Y.C. and Y.D.; writing—original draft preparation, Q.Y.; writing—review and editing, Q.Y. and S.Z.; visualization, Q.Y.; supervision, S.Z. All authors have read and agreed to the published version of the manuscript.

Funding: This research received no external funding.

Data Availability Statement: Not applicable.

Conflicts of Interest: The authors declare no conflicts of interest.

References

1. Bin Mohamed Rehan, M.S.; Rousseau, J.; Fontaine, S.; Gong, X.J. Experimental Study of the Influence of Ply Orientation on DCB Mode-I Delamination Behavior by Using Multidirectional Fully Isotropic Carbon/Epoxy Laminates. *Composite Structures* **2017**, *161*, 1–7, doi:10.1016/j.compstruct.2016.11.036.
2. Hegde, S.; Satish Shenoy, B.; Chethan, K.N. Review on Carbon Fiber Reinforced Polymer (CFRP) and Their Mechanical Performance. *Materials Today: Proceedings* **2019**, *19*, 658–662, doi:10.1016/j.matpr.2019.07.749.

3. Huo, R.; Chen, L.; Liu, J.; Peng, D. The Application of Transfer Matrix Method in Acoustic Performance Analysis of Composite Materials and Acoustic Protection Design of Ship. *IOP Conf. Ser.: Mater. Sci. Eng.* **2019**, *544*, 012047, doi:10.1088/1757-899X/544/1/012047.
4. Wang, Z.W.; Zhao, J.P.; Zhang, X. Finite Element Analysis of Composite Laminates Subjected to Low-Velocity Impact Based on Multiple Failure Criteria. *Mater. Res. Express* **2018**, *5*, 065320, doi:10.1088/2053-1591/aacca3.
5. May, M.; Rupakula, G.D.; Matura, P. Non-Polymer-Matrix Composite Materials for Space Applications. *Composites Part C: Open Access* **2020**, *3*, 100057, doi:10.1016/j.jcomc.2020.100057.
6. Langat, R.K.; De Luycker, E.; Cantarel, A.; Rakotondrabe, M. Integration Technology with Thin Films Co-Fabricated in Laminated Composite Structures for Defect Detection and Damage Monitoring. *Micromachines* **2024**, *15*, 274, doi:10.3390/mi15020274.
7. Singh, A.P.; Sharma, M.; Singh, I. A Review of Modeling and Control during Drilling of Fiber Reinforced Plastic Composites. *Composites Part B: Engineering* **2013**, *47*, 118–125, doi:10.1016/j.compositesb.2012.10.038.
8. Vishwakarma, A.; Behera, A.; Thawre, M.M.; Ballal, A.R. Effect of Thickness Variation on Static Behaviour of Carbon Fiber Reinforced Polymer Multidirectional Laminated Composite. *Mater. Res. Express* **2019**, *6*, 115312, doi:10.1088/2053-1591/ab44fa.
9. Shyha, I.; Soo, S.L.; Aspinwall, D.; Bradley, S. Effect of Laminate Configuration and Feed Rate on Cutting Performance When Drilling Holes in Carbon Fibre Reinforced Plastic Composites. *Journal of Materials Processing Technology* **2010**, *210*, 1023–1034, doi:10.1016/j.jmatprotec.2010.02.011.
10. Singh, T.J.; Samanta, S. Characterization of Kevlar Fiber and Its Composites: A Review. *Materials Today: Proceedings* **2015**, *2*, 1381–1387, doi:10.1016/j.matpr.2015.07.057.
11. McConnell, V.P. Ballistic Protection Materials a Moving Target. *Reinforced Plastics* **2006**, *50*, 20–25, doi:10.1016/S0034-3617(06)71187-0.
12. Ameri, B.; Moradi, M.; Mohammadi, B.; Salimi-Majd, D. Investigation of Nonlinear Post-Buckling Delamination in Curved Laminated Composite Panels via Cohesive Zone Model. *Thin-Walled Structures* **2020**, *154*, 106797, doi:10.1016/j.tws.2020.106797.
13. Cairns, D.S.; Nelson, J.W.; Woo, K.; Miller, D. Progressive Damage Analysis and Testing of Composite Laminates with Fiber Waves. *Composites Part A: Applied Science and Manufacturing* **2016**, *90*, 51–61, doi:10.1016/j.compositesa.2016.03.005.
14. Mehdikhani, M.; Gorbatikh, L.; Verpoest, I.; Lomov, S.V. Voids in Fiber-Reinforced Polymer Composites: A Review on Their Formation, Characteristics, and Effects on Mechanical Performance. *Journal of Composite Materials* **2019**, *53*, 1579–1669, doi:10.1177/0021998318772152.
15. Woo, K.; Nega, B.F.; Cairns, D.S.; Lua, J. Delamination Behavior of L-Shaped Composite Beam with Manufacturing Defects. *J Mech Sci Technol* **2020**, *34*, 3709–3720, doi:10.1007/s12206-020-0823-y.
16. Li, J.G.; Liu, P.F.; Chu, J.K. Finite Element Analysis of Delamination Behaviors of Composite Laminates under Hygrothermal Environment Using Virtual Crack Closure Technique. *J Fail. Anal. and Preven.* **2019**, *19*, 147–153, doi:10.1007/s11668-019-00582-5.
17. Kharghani, N.; Guedes Soares, C. Behavior of Composite Laminates with Embedded Delaminations. *Composite Structures* **2016**, *150*, 226–239, doi:10.1016/j.compstruct.2016.04.042.
18. Yamanaka, T.; Heidari-Rarani, M.; Lessard, L.; Feret, V.; Hubert, P. A New Finite Element Method for Modeling Delamination Propagation without Additional Degrees of Freedom. *Composite Structures* **2016**, *147*, 82–98, doi:10.1016/j.compstruct.2016.03.040.
19. Jin, F.; Xu, P.; Xia, F.; Liang, H.; Yao, S.; Xue, J. Buckling of Composite Laminates with Multiple Delaminations: Part I Theoretical and Numerical Analysis. *Composite Structures* **2020**, *250*, 112491, doi:10.1016/j.compstruct.2020.112491.
20. Higuchi, R.; Warabi, S.; Ishibashi, W.; Okabe, T. Experimental and Numerical Investigations on Push-out Delamination in Drilling of Composite Laminates. *Composites Science and Technology* **2020**, *198*, 108238, doi:10.1016/j.compscitech.2020.108238.
21. Geng, D.; Liu, Y.; Shao, Z.; Lu, Z.; Cai, J.; Li, X.; Jiang, X.; Zhang, D. Delamination Formation, Evaluation and Suppression during Drilling of Composite Laminates: A Review. *Composite Structures* **2019**, *216*, 168–186, doi:10.1016/j.compstruct.2019.02.099.
22. Hocheng, H.; Chen, C.C.; Tsao, C.C. Prediction of Critical Thrust Force for Tubular Composite in Drilling-Induced Delamination by Numerical and Experimental Analysis. *Composite Structures* **2018**, *203*, 566–573, doi:10.1016/j.compstruct.2018.07.051.
23. Ouyang, T.; Sun, W.; Bao, R.; Tan, R. Effects of Matrix Cracks on Delamination of Composite Laminates Subjected to Low-Velocity Impact. *Composite Structures* **2021**, *262*, 113354, doi:10.1016/j.compstruct.2020.113354.
24. Sivakumar, V.; Gautham Barathwaj, P.; Santosh Kumar, M.; Srikar, D. Delamination Propagation Study on Aircraft Composite Rib Subjected to Fatigue Loading. *J Fail. Anal. and Preven.* **2020**, *20*, 1351–1363, doi:10.1007/s11668-020-00936-4.

25. Gong, Y.; Zhao, L.; Zhang, J.; Hu, N. A Novel Model for Determining the Fatigue Delamination Resistance in Composite Laminates from a Viewpoint of Energy. *Composites Science and Technology* **2018**, *167*, 489–496, doi:10.1016/j.compscitech.2018.08.045.
26. Gong, Y.; Zhao, L.; Zhang, J.; Hu, N.; Zhang, C. Development of a Standardized Test Procedure and an Improved Data Reduction Method for the Mixed-Mode I/II Delamination in Composite Laminates. *Composites Science and Technology* **2021**, *201*, 108488, doi:10.1016/j.compscitech.2020.108488.
27. Carrino, S.; Maffezzoli, A.; Scarselli, G. Active SHM for Composite Pipes Using Piezoelectric Sensors. *Materials Today: Proceedings* **2021**, *34*, 1–9, doi:10.1016/j.matpr.2019.12.048.
28. Raišutis, R.; Kažys, R.; Žukauskas, E.; Mažeika, L.; Vladišauskas, A. Application of Ultrasonic Guided Waves for Non-Destructive Testing of Defective CFRP Rods with Multiple Delaminations. *NDT & E International* **2010**, *43*, 416–424, doi:10.1016/j.ndteint.2010.04.001.
29. Cantero-Chinchilla, S.; Malik, M.K.; Chronopoulos, D.; Chiachío, J. Bayesian Damage Localization and Identification Based on a Transient Wave Propagation Model for Composite Beam Structures. *Composite Structures* **2021**, *267*, 113849, doi:10.1016/j.compstruct.2021.113849.
30. De Luca, A.; Perfetto, D.; De Fenza, A.; Petrone, G.; Caputo, F. Guided Waves in a Composite Winglet Structure: Numerical and Experimental Investigations. *Composite Structures* **2019**, *210*, 96–108, doi:10.1016/j.compstruct.2018.11.048.
31. Munian, R.K.; Roy Mahapatra, D.; Gopalakrishnan, S. Ultrasonic Guided Wave Scattering Due to Delamination in Curved Composite Structures. *Composite Structures* **2020**, *239*, 111987, doi:10.1016/j.compstruct.2020.111987.
32. Hunten, K.A.; Barnard Feeney, A.; Srinivasan, V. Recent Advances in Sharing Standardized STEP Composite Structure Design and Manufacturing Information. *Computer-Aided Design* **2013**, *45*, 1215–1221, doi:10.1016/j.cad.2013.05.001.
33. Seeger, J.; Wolf, K. Multi-Objective Design of Complex Aircraft Structures Using Evolutionary Algorithms. *Proceedings of the Institution of Mechanical Engineers, Part G: Journal of Aerospace Engineering* **2011**, *225*, 1153–1164, doi:10.1177/0954410011411384.
34. Rao, J.; Ratassepp, M.; Lisevych, D.; Hamzah Caffoor, M.; Fan, Z. On-Line Corrosion Monitoring of Plate Structures Based on Guided Wave Tomography Using Piezoelectric Sensors. *Sensors* **2017**, *17*, 2882, doi:10.3390/s17122882.
35. He, J.; Huo, H.; Guan, X.; Yang, J. A Lamb Wave Quantification Model for Inclined Cracks with Experimental Validation. *Chinese Journal of Aeronautics* **2021**, *34*, 601–611, doi:10.1016/j.cja.2020.02.010.
36. Shoja, S.; Berbyuk, V.; Boström, A. Delamination Detection in Composite Laminates Using Low Frequency Guided Waves: Numerical Simulations. *Composite Structures* **2018**, *203*, 826–834, doi:10.1016/j.compstruct.2018.07.025.
37. Sha, G.; Xu, H.; Radzieński, M.; Cao, M.; Ostachowicz, W. Wavelet-Aided Guided Wavefield Imaging of Delaminations in Laminated Composite Plates. *Smart Mater. Struct.* **2020**, *29*, 105029, doi:10.1088/1361-665X/aba81b.
38. Michalcová, L.; Hron, R. Quantitative Evaluation of Delamination in Composites Using Lamb Waves. *IOP Conf. Ser.: Mater. Sci. Eng.* **2018**, *326*, 012006, doi:10.1088/1757-899X/326/1/012006.
39. Feng, B.; Ribeiro, A.L.; Ramos, H.G. Interaction of Lamb Waves with the Edges of a Delamination in CFRP Composites and a Reference-Free Localization Method for Delamination. *Measurement* **2018**, *122*, 424–431, doi:10.1016/j.measurement.2017.10.016.
40. Huang, L.; Zeng, L.; Lin, J.; Zhang, N. Baseline-Free Damage Detection in Composite Plates Using Edge-Reflected Lamb Waves. *Composite Structures* **2020**, *247*, 112423, doi:10.1016/j.compstruct.2020.112423.
41. Zhang, H.; Hua, J.; Gao, F.; Lin, J. Efficient Lamb-Wave Based Damage Imaging Using Multiple Sparse Bayesian Learning in Composite Laminates. *NDT & E International* **2020**, *116*, 102277, doi:10.1016/j.ndteint.2020.102277.
42. Zhao, X.; Royer, R.L.; Owens, S.E.; Rose, J.L. Ultrasonic Lamb Wave Tomography in Structural Health Monitoring. *Smart Mater. Struct.* **2011**, *20*, 105002, doi:10.1088/0964-1726/20/10/105002.
43. Huang, L.; Zeng, L.; Lin, J.; Luo, Z. An Improved Time Reversal Method for Diagnostics of Composite Plates Using Lamb Waves. *Composite Structures* **2018**, *190*, 10–19, doi:10.1016/j.compstruct.2018.01.096.
44. Wang, S.; Wu, W.; Shen, Y.; Liu, Y.; Jiang, S. Influence of the PZT Sensor Array Configuration on Lamb Wave Tomography Imaging with the RAPID Algorithm for Hole and Crack Detection. *Sensors* **2020**, *20*, 860, doi:10.3390/s20030860.
45. Guo, J.; Zeng, X.; Liu, Q.; Qing, X. Lamb Wave-Based Damage Localization and Quantification in Composites Using Probabilistic Imaging Algorithm and Statistical Method. *Sensors* **2022**, *22*, 4810, doi:10.3390/s22134810.
46. Huo, H.; He, J.; Guan, X. A Bayesian Fusion Method for Composite Damage Identification Using Lamb Wave. *Structural Health Monitoring* **2021**, *20*, 2337–2359, doi:10.1177/1475921720945000.

 doi:10.20944/preprints202404.1308.v1